J Mater Sci (2011) 46:6065–6074
DOI 10.1007/s10853-011-5568-7

Self-nanoscaling of the soft magnetic phase in bulk SmCo/Fe nanocomposite magnets

Chuanbing Rong · Ying Zhang · Narayan Poudyal · Izabela Szlufarska · Rainer J. Hebert · M. J. Kramer · J. Ping Liu

Received: 18 January 2011 / Accepted: 16 April 2011 / Published online: 3 May 2011

Abstract Fabrication of bulk nanocomposite materials, which contain a magnetically hard phase and a magnetically soft phase with desired nanoscale morphology and composition distribution has proven to be challenging. Here we demonstrate that SmCo/Fe(Co) hard/soft nanocomposite materials can be produced by distributing the soft magnetic α-Fe(Co) phase particles homogenously in a hard magnetic SmCo phase matrix through a combination of high-energy ball milling and a warm compaction. Severe plastic deformation during the ball milling results in nanoscaling of the soft phase with size reduction from micrometers to ~15 nm. Up to 35% of the soft phase can be incorporated into the composites without coarsening. This process produces fully dense bulk isotropic nanocomposite materials with remarkable energy-product enhancement (up to 300%) owing to effective inter-phase exchange coupling.

C. Rong · Y. Zhang · N. Poudyal · J. P. Liu (✉)
Department of Physics, University of Texas at Arlington, Arlington, TX 76019, USA
e-mail: pliu@uta.edu

Y. Zhang · M. J. Kramer
Division of Materials Science and Engineering, Ames Laboratory, Iowa State University, Ames, IA 50011, USA

I. Szlufarska
Department of Materials Science & Engineering, University of Wisconsin at Madison, Madison, WI 53706, USA

R. J. Hebert
Department of Chemical, Materials & Biomolecular Engineering, University of Connecticut, Storrs, CT 06269, USA

Introduction

Despite tremendous efforts dedicated to searching for new permanent magnetic materials, no single compound or alloy has yet been discovered which possesses all the properties of an ideal permanent magnet. These properties include high magnetization, high Curie temperature, and high anisotropy. It is also desirable that these excellent properties are achieved at a low cost. Sm–Co intermetallic compounds (including $SmCo_5$, Sm_2Co_{17}, and Sm_2Co_7) have the highest magnetocrystalline anisotropy ($\sim 10^7$ erg/cc) and the highest Curie temperatures (up to 1190 K) among all the permanent magnets discovered to date [1]. For these reasons, Sm–Co based magnets are the permanent magnets of choice for high temperature applications. One outstanding challenge of the currently available Sm–Co based magnets is their relatively low saturation magnetization, M_s, as compared to Nd–Fe–B based magnets. Consequently utilizaton of Sm–Co has been restricted in high power density applications, such as wind power turbines and electric motors in hybrid vehicles. Since Nd–Fe–B based magnets have a relatively low Curie temperature ($\sim$580 K), utilization of these materials in high power density applications requires cooling, which in turn reduces the overall system efficiency. In order to take advantage of the considerably higher operating temperature attainable with Sm–Co magnets, the M_s value of this composite needs to be raised to boost the energy product, $(BH)_{max}$, the figure of merit of a permanent magnet. To reduce the materials costs, it is desirable to lower the concentration of Sm and Co in the magnetic material since the elements are expensive.

One solution to both the M_s and the material cost problems is to fabricate nanocomposite magnets that contain a magnetically hard phase (e.g., Sm–Co) and a

magnetically soft phase (e.g., Fe) with desired nanoscale morphology and composition distribution [2–4]. If the two phases have a strong exchange coupling, the hard magnetic phase will provide high coercivity and the soft magnetic phase will provide high magnetization to the composite. This type of nanocomposite magnets can therefore achieve simultaneously an increase in M_s (and therefore also $(BH)_{max}$) and a reduction in the materials cost (through addition of Fe). The energy product of such composite magnets depends not only on the intrinsic properties of the magnetic phases, but also on their morphology (e.g., dimensions of the soft phase, a relative fraction of the two phases and their distribution). Theoretical calculations have predicted that the energy product of an ideal nanocomposite system can be up to 100% higher than that of the currently available Nd–Fe–B magnets [5, 6]. The concept of exchange-coupled nanocomposite magnets has opened an avenue to the design of new materials with superior magnetic properties. Experimental efforts in the past two decades have demonstrated that energy product enhancement can be achieved in low dimensional hard/soft magnetic systems including physically deposited thin films [7–9], rapidly quenched ribbons [10–12], mechanically milled powders [13–15], and self-assembled and core–shell nanoparticle systems [16–18]. However, scaling these processes up to bulk materials remains an outstanding challenge. Traditional processing techniques such as casting and sintering are ill-suited for producing nanostructured bulk materials since long anneals at high temperatures inevitably lead to excessive grain growth. Stable grain size in fully dense nanocomposite magnets have been achieved by non-traditional approaches, which include spark plasma sintering of NdFeB [19, 20] and FePt [21], shock compaction of nanoscale granular Nd–Fe–B granular ribbons [22], and warm compaction of FePt–Fe_3O_4 nanoparticles (particle size of 4–6 nm) [23]. In particular, we have recently demonstrated that bulk SmCo/Fe(Co) nanocomposite magnets can be fabricated with greatly enhanced energy products compared to single-phase counterparts by high-energy ball milling and warm compaction processing [24, 25]. In this report, we extend the investigation to the evolution of the micron- and nanoscale morphology during the deformation and the heat treatments, in order to understand both the mechanisms that underlie nanoscaling of the soft phase, and correlation between the morphology and the magnetic properties of the nanocomposite.

Experimental approach

The raw materials used in our study were commercially available powders of α-Fe (Sigma-Aldrich Co., <10 μm), and $SmCo_5$ (Alfa Aesar, ~45 μm), or Sm_2Co_7 (Sigma-Aldrich Co., ~45 μm), or Sm_2Co_{17} (Electron Energy Corp., ~45 μm). The Sm–Co compounds and α-Fe metal were used as magnetically hard and soft phases, respectively. The nanocomposite powders were prepared by high energy ball milling of the hard and soft magnetic phase particles in a hardened steel grinding vial using a SPEX 8000M Mixer/Mill. The balls are made of 440C hardened steel and have a diameter around 9 mm (McMaster-Carr). The weight ratio of soft phase to hard phase was varied from 0 to 50%. The weight ratio of sample to ball was around 1:20–30. The milling time was varied from 0.5 to 10 h. The ball milling process has two purposes: to mix the two phases and to reduce the particle sizes via severe plastic deformation. Consolidation was achieved by warm compaction of the milled mixtures at different temperatures (from room temperature to 700 °C) under a nominally hydrostatic pressure of ~2.5 GPa. Fully dense bulk samples were obtained at temperatures around 500 °C. The final bulk samples were pellet-shaped with a diameter of 6 mm and a pellet height of 1.5 mm. The geometric density was calculated by assuming a regular shape of the compacted sample.

The morphology and crystalline structure were characterized by electron microscopies and X-ray diffraction (XRD). Here scanning electron microscopy (SEM) and backscattered electron (BSE) images were collected using JEOL JSM-5910LV SEM. Transmission electron microscopy (TEM) observation was performed on 200 kV FEI Tecnai G2 F20 scanning transmission electron microscopy (STEM) equipped with a post column Gatan Imaging Filter (GIF) and High Angle Annual Dark Field (HAADF) detector. TEM samples were made by mechanical polishing, dimpling, and ion milling, and liquid nitrogen was used during ion milling to protect the sample. Energy-filtered transmission electron microscopy (EFTEM) mappings with nanometer resolution and higher energy resolution provide reliable maps of the soft-phase distribution. Using characteristic ionization edges of l_3 708 eV for Fe and l_3 779 eV for Co and M_5 1080 eV for Sm, quantitative two-dimensional elemental distribution maps can be obtained in a fast parallel fashion with nanometer resolution and high chemical accuracy. Three-window method is used when collecting EFTEM mapping, at each image pixel a background is fitted to the two pre edge images and subtracted from the post edge image, to obtain the elemental distribution image. XRD patterns were collected on a Rigaku Ultima IV using Cu K_α radiation. Magnetic properties were measured with a superconducting quantum interference device (SQUID) magnetometer (Quantum Design Inc.) with a maximum applied field of 70 kOe.

Since the field inside a specimen is always different from the applied field because of the inside magnetization,

we need to correct the measured demagnetization curves using a demagnetization factor to obtain the correct energy-product values $(BH)_{max}$ of the bulk samples. However, theoretical demagnetization factors can be calculated only for homogeneous media with regular shapes. Therefore, we determined the demagnetization factor experimentally by the following processes: The demagnetization curves for the disk-shaped sample were measured along directions parallel and perpendicular to the cylindrical axis of the disk using the SQUID magnetometer. The measured demagnetization curves along different directions are usually not same due to the geometry of the bulk samples. The slope of the demagnetization curve along the direction parallel to the cylindrical axis of the disk is smaller than that of other directions due to the large demagnetization factor. In principle, the demagnetization curves should be the same along different directions of the sample after demagnetization corrections for the isotropic magnets. Assuming $N_c + 2N_a = 1$ [26], the demagnetization factor parallel (N_c) and perpendicular (N_a) to the axis of the disk can be obtained by fitting the two modified demagnetization curves measured along different directions using different demagnetization factors. For the best fitting, when the two corrected demagnetization curves match each other, the used demagnetization factor is the right one for the bulk sample. Therefore, the true energy product of the bulks can be calculated.

Results and discussion

Self-nanoscaling of the soft phase through severe plastic deformation

The effect of milling time on the microstructure of the two-phase systems was monitored by the BSE technique and EFTEM (Fig. 1). For milling time of 30 min or less, the BSE images (see Fig. 1a–c) show a moderate particle size commutation. For longer milling times, imaging of the microstructure required the higher magnification of the TEM. In particular, EFTEM can rapidly produce composition maps with nanometer resolution showing distinct two-phase regions. As shown in Fig. 1d, the EFTEM analysis revealed an unusual morphology that developed after ~30 min of milling. With increasing milling time, the soft magnetic phase, which started off as equiaxed micrometer-sized α-Fe particles, became narrow and elongated (Fig. 1e). With further milling, the nanoscale α-Fe strips began to break up into isolated equiaxed nanoscale particles. After ~4 h of milling, the result was a homogenously distributed magnetically soft particulate phase embedded in the hard-phase matrix with sizes as small as 5 nm (Fig. 1f). The milling process not only induces the elongation and eventual break-down of the Fe phase into nanoparticles, but furthermore amorphization of the Sm–Co matrix phase.

A schematic representation of the microstructural evolution is shown in Fig. 1g–j. This "self-nanoscaling" phenomenon of the soft-phase particles, accompanied by a size reduction from micrometers to nanometers, can be attributed to large strain deformation and plastic instabilities in the Fe phase. The large strain deformation of two-phase systems has been studied mainly with wire-drawing [27–30], ball-milling [31], and repeated cold rolling and folding [32–36]. The break-up of layers during large strain composite deformation is not limited to metallic materials, but was also observed for ceramic layers in a ceramic composite by Chen et al. [35]. Different microstructural responses of two-phase materials to large strain deformation have been observed. One morphology change involves a continuous decrease in one dimension of the individual phases while their contiguity is not disrupted. This morphology evolution has been referred to as "codeformation". Quite an opposite situation is observed when one of the phases ruptures into fragments that are embedded in the second—typically softer—phase [37]. The rupture process follows plastic instability [38]. Flow stress or hardness differences between the phases induce tensile stresses for the harder phase that induces necking [38–41]. A comparison between tensile yield strengths of bcc iron and $SmCo_5$ or Sm_2Co_{17} samples shows that the strength of the Sm–Co phases of approximately 350–400 MPa exceeds the yield strength of iron of about 250 MPa, but that the strength ratio of the iron and Sm–Co phases is less than two. Based on an empirical rule that co-deformation is favored if the strength ratio of the phases is less than approximately three [42] the mixture of Fe and Sm–Co phases should reveal a two-phase morphology evolution that is closer to a co-deformation behavior than a fracture–rupture behavior. Figure 1a and b indeed agrees with the prediction of co-deformation. Figure 2 additionally shows a bright-field TEM image of the powder mixture after 30 min of milling. The layers having mix of bright–dark contrast owing to their crystalline nature is the soft magnetic Fe phase which is continuous over the viewing area; one layer clearly reveals multiple necking as indicated with arrows in the figure. The necking at this stage of the deformation, when the layers have already undergone significant reduction in thickness to less than 50 nm, suggests that the flow stress ratio is changing at this extended deformation stage. Several factors could contribute to changes in mechanical properties of the two phases relative to each other: the ball-milling process induces mixing between the iron and Sm–Co phases. Moreover, the Sm–Co phase transforms to an amorphous phase yet the Fe remains crystalline. Ball-milling induced amorphization of

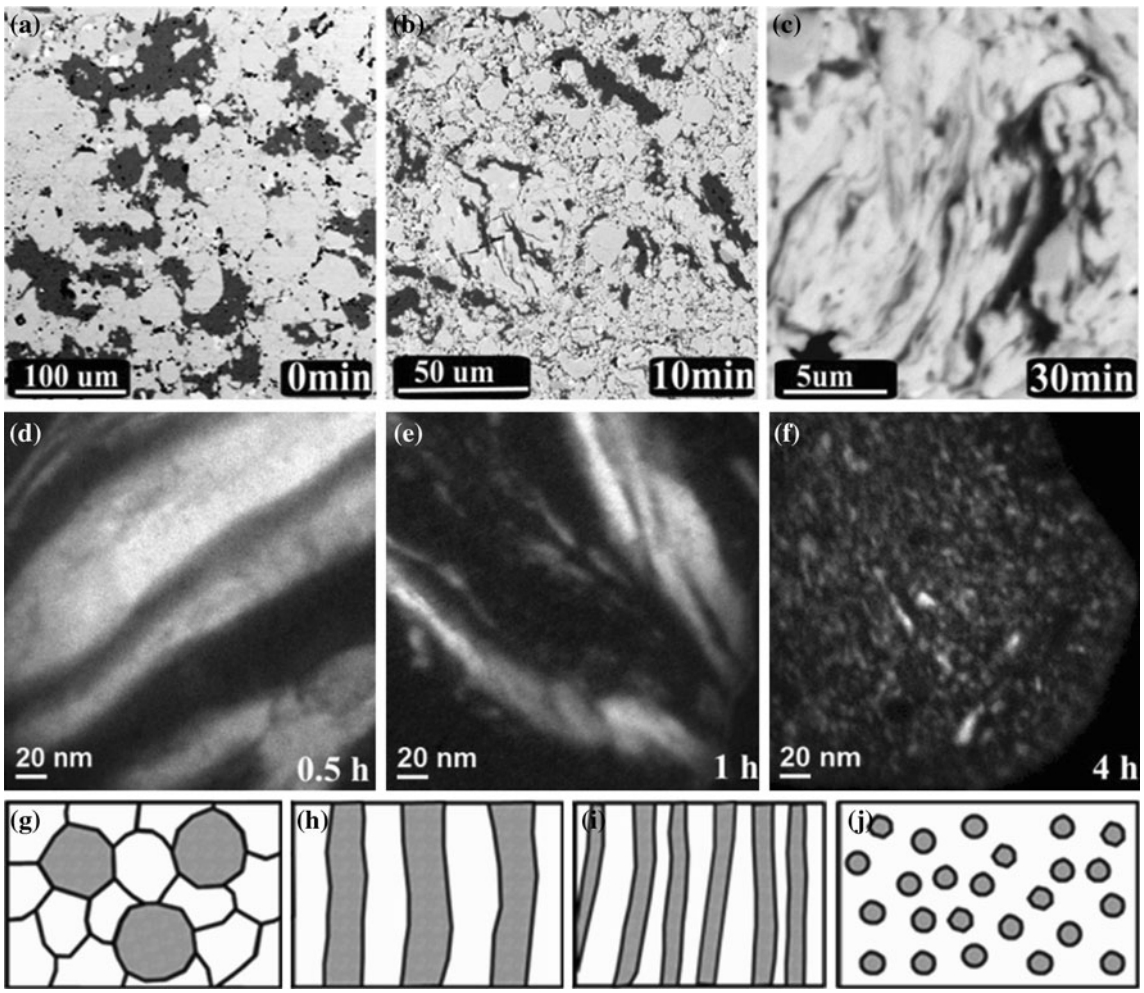

Fig. 1 Morphology evolution during the deformation. BSE images of **a** a mixture of $SmCo_5$ + 20 wt% Fe, and the mixture after milling for **b** 10 and **c** 30 min. Fe strips (dark contrast) can be observed in samples milled for more than 30 min; EFTEM showing Fe maps of the samples milled for **d** 30 min, **e** 1 h, and **f** 4 h, respectively. High Fe regions have bright contrast. The Fe strips become thinner with increasing milling time; Schematic show of the microstructure evolution during the deformation: **g** mixed micron size powder particles, **h** formation of elongated Fe strips upon deformation, **i** strips with reduced size upon further deformation, **j** thinned strips broken into equiaxed grains

intermetallic phases has been observed, for example, for Y–Co powder mixtures [43]. The Fe layers show a lot of contrast, indicating that they may be strain hardening. Both mixing and solid-state amorphization are expected to change the mechanical properties of the two phases and of the interface significantly, but the impact of driven mixing at the interfaces during ball-milling and amorphization on the necking behavior requires further in-depth studies.

Milling of the powder mixture leads to formation of an amorphous matrix that contains bcc (Fe,Co) nanoparticles. Figure 3 shows the selected area electron diffraction (SAED) and XRD patterns of the $SmCo_5$ + 20 wt% Fe powders milled for 4 h. As one can see that the electron and X-ray diffractions only shows the (110), (200), and (211) rings/peaks for the bcc α-(Fe,Co) phase. The very broad and weak peak near 25°–55° should belong to the Sm–Co phase, which suggests that the Sm–Co phase is in amorphous structure after the milling. Annealing of the as-milled powder can then transform the amorphous Sm–Co matrix into a crystalline matrix. The annealing conditions must be controlled to crystallize the desired hard magnetic phase, while minimizing grain growth or coarsening of the magnetic soft phase. Fortunately, the size of the magnetic soft-phase particles remains below 10–15 nm after the optimized annealing for the 4 h milled samples. Figure 4 indeed demonstrates that the size of the soft magnetic particles increases only slightly with annealing at 550 °C and remains at about 12 nm. Here the grain size was estimated from the XRD patterns using Williamson–Hall plot [44]. It should be mentioned that the grain size determined by XRD patterns and TEM images has been compared and good agreement is obtained (the difference

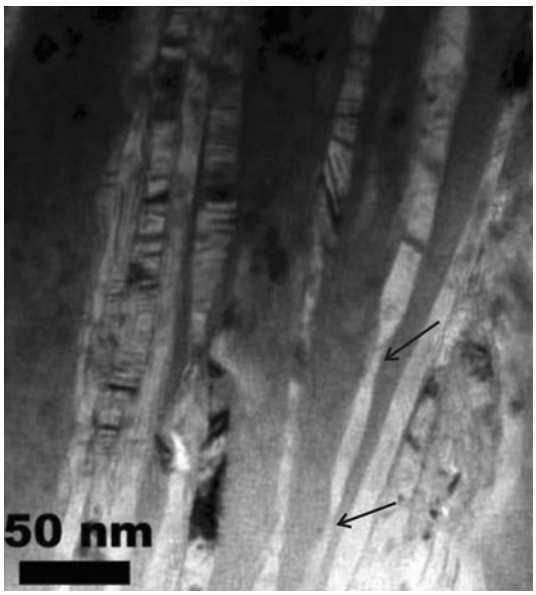

Fig. 2 The bright-field TEM image of the soft-phase trips formed after 30 min milling of the $SmCo_5$/Fe composite system

is only about 1–2 nm). The size of the soft magnetic phase is below the critical dimension ($\sim$15 nm), above which the exchange coupling becomes less effective. This critical dimension was estimated by considering the hard-phase domain wall thickness and soft-phase magnetic properties [3, 5, 45–48]. Without the grain size reduction through ball milling, the BCC particle size is too large for effective exchange coupling. Figure 5 shows the demagnetization curves of the optimally annealed $SmCo_5$ + 20 wt% Fe samples whose starting powders were milled for different periods of times. For samples milled for less than 2 h there is a noticeable kink in the demagnetization loops, indicating a de-coupled two-phase demagnetization behavior due to the too large soft-phase grains. Samples milled longer than 2 h exhibit smooth demagnetization curves, which confirms the uniform nanoscale morphology. Additional milling (for up to 10 h) did not lead to any improvement in the energy product because of the reduced hard-phase thermal stability. It should be mentioned that the saturation magnetization increases with increasing milling time. This is consistent with the measured interdiffusion of Co into the Fe and the fact that the solid-solution does have a higher M_s [24].

Effect of the soft-phase fraction and composition

Increasing magnetization through exchange coupling requires a substantial fraction of a soft magnetic phase. However, it is experimentally challenging to distribute a large volume fraction of a soft phase in the matrix while maintaining the particle size below the critical size for

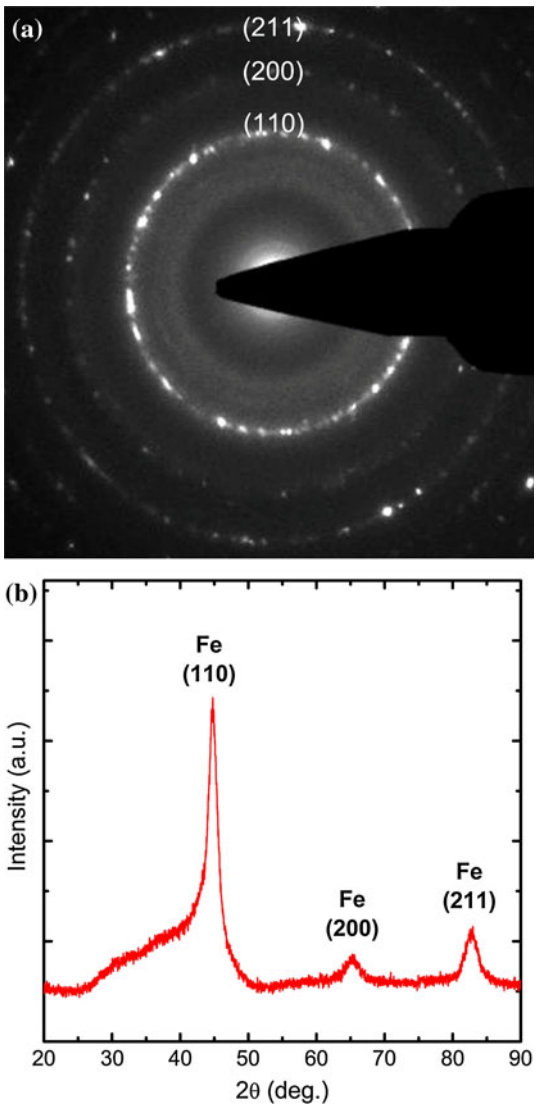

Fig. 3 SAED and XRD patterns of the $SmCo_5$ + 20 wt% Fe powders milled for 4 h

exchange coupling. In practice, any increase in the soft-phase fraction is accompanied by a reduction in coercivity of the composite magnets. To measure the trade-off between the magnetization and coercivity, we investigated the soft-phase fraction dependence of magnetic properties of the $SmCo_5$/Fe system.

Figure 6 shows the EFTEM Fe maps obtained for samples with a varying α-Fe content in the $SmCo_5$/Fe nanocomposites. We were able to demonstrate a homogeneous distribution of the soft phase for α-Fe content of up to about 30 wt%. The XRD analysis shown in Fig. 7 confirms that the soft-phase portion in the optimally annealed samples increases with increasing weight fraction of Fe based on the increase of the relative intensity of the diffraction peak of α-Fe phase. Increasing the weight fraction beyond 30% impeded the nanoscaling process,

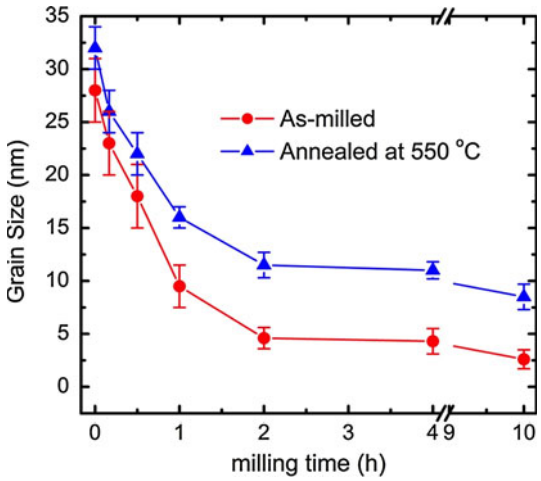

Fig. 4 The dependence of average α-Fe grain size of the as-milled and 550 °C annealed $SmCo_5$ + 20 wt% Fe powders on milling time where the grain size was estimated from the XRD patterns using Williamson–Hall plot

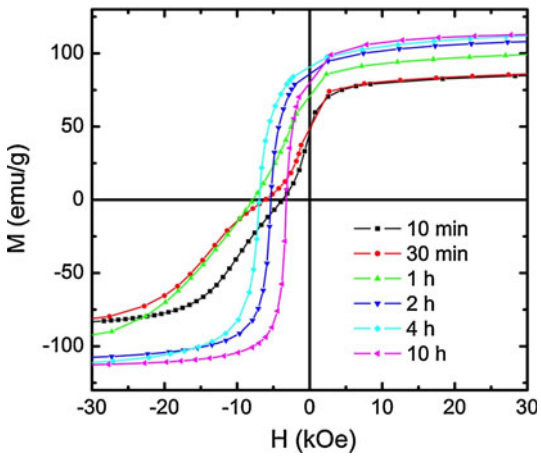

Fig. 5 Demagnetization curves of the composite samples milled for different time after annealing at 550 °C for 30 min. Since the magnetization loops are symmetrical in shape, only the demagnetization halves are plotted

leaving large soft-phase strips that cause a significant reduction of the coercivity and therefore of the energy product. This reduction in coercivity is demonstrated in Fig. 8, which shows demagnetization curves of the nanocomposite magnets with different amount of the soft phase. As expected that while an increase in soft-phase content reduces the coercivity, it leads to an increase in saturation magnetization. Figure 9 summarizes the effects of the soft-phase fraction on the magnetization and coercivity. The opposite trends in the magnetization and the coercivity leads to a peak in the energy product value of 18.3 MGOe at ~20 wt% Fe (Fig. 10). It should be noted that the gain in saturation magnetization upon soft-phase addition in a hard/soft nanocomposite should follow a simple linear relationship if there is no interdiffusion between the magnetically hard and soft phases [3].

$$M_{\text{com}} = xM_{\text{soft}} + (1-x)M_{\text{hard}} \quad (1)$$

where M_{com}, M_{soft}, and M_{hard} are saturation magnetization for the composite, the soft phase and the hard phase, respectively, and x is the soft-phase fraction. This linear correlation was plotted as the dashed line in Fig. 9 for the $SmCo_5$/Fe system. The experimental data, which also follows a linear with x, is plotted as a dotted line. A significant deviation was observed between the measured magnetization and the values given by Eq. 1, with the measured values being consistently higher. This deviation should be caused by the interdiffusion of Co and Fe in the nanocomposite. To confirm the interdiffusion of Co–Fe during the warm compaction, we performed the 3DAP analysis for the compacted SmCo/Fe bulks as reported in Ref. [24] and the parallel electron energy loss spectroscopy (PEELS) line scans as reported in Ref. [25]. After the pre-compaction annealing and the warm compaction, the pure α-Fe phase became a FeCo alloy with higher magnetization, as we will discuss in "Effect of compaction and interface conditions" section. It should be noted that the wavelike compositional profile of the soft phase forms the graded interface between the hard/soft interface, which could result in better exchange coupling between the two phases of nanocomposite magnets [49, 50].

Effect of the hard-phase composition

In addition to the effects of the soft-phase content on magnetic properties, we have also carried out investigations of the role the hard phase plays in the Sm_2Co_7 and Sm_2Co_{17}-based nanocomposite systems. Figure 10 shows the dependence of the energy product on soft-phase content in three nanocomposite systems that contain different hard phases. A more favorable situation has been found in the Sm_2Co_7-based system. The energy product peaks at 17 MGOe when 35 wt% Fe was added, which represents a ~300% enhancement compared to the single-phase counterpart (~4 MGOe). This remarkable energy product enhancement can be attributed to the fact that Sm_2Co_7 has a relatively low magnetocrystalline anisotropy as compared to $SmCo_5$ [1]. Therefore, the Sm_2Co_7-based composites have a larger critical soft-phase dimension according to the anti-correlation between the hard-phase anisotropy constant and the critical soft-phase dimension [3] and these composites are expected to tolerate more soft-phase and soft-phase agglomeration. Our TEM observations have confirmed this phenomenon [25]. Figure 11 shows the energy product enhancement achieved in this work for the optimized $SmCo_5$/FeCo and Sm_2Co_7/Fe systems. Data for the Sm_2Co_{17}-based systems is not shown because the

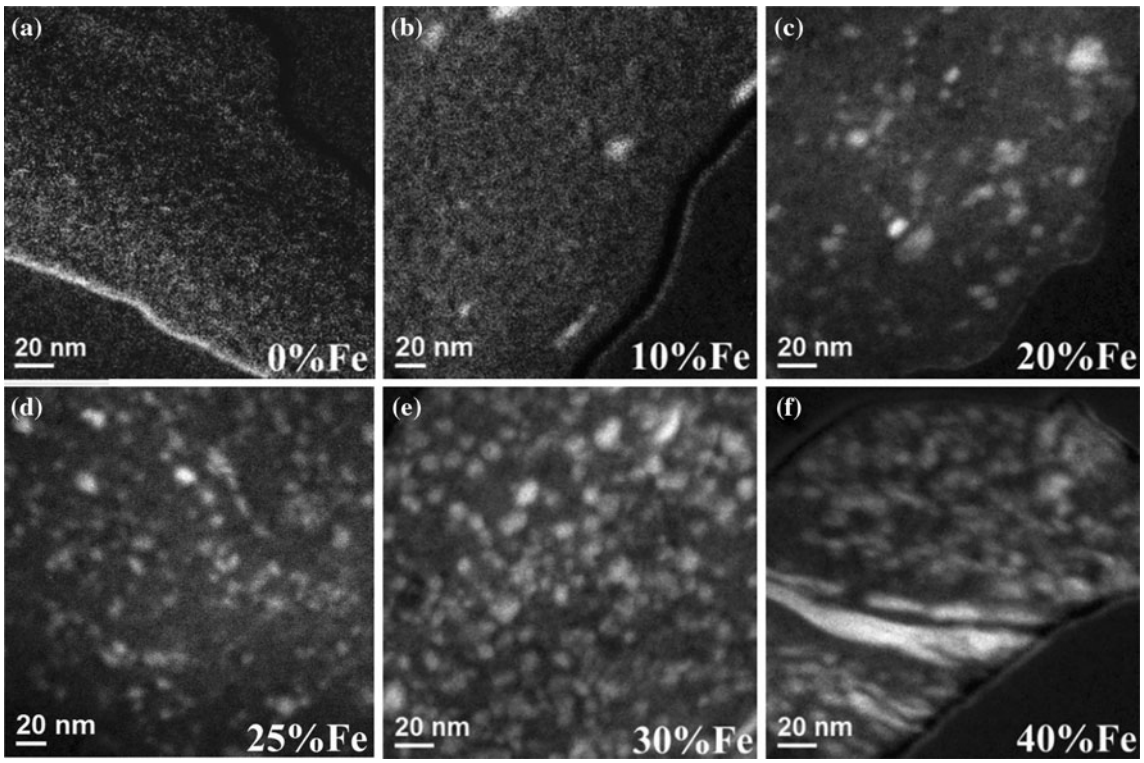

Fig. 6 Morphology and magnetic properties upon increased soft-phase fraction. EFTEM Fe maps of the $SmCo_5$/Fe samples with different Fe content: **a** 0 wt% Fe, **b** 10 wt% Fe, **c** 20 wt% Fe, **d** 25 wt% Fe, **e** 30 wt% Fe, **f** 40 wt% Fe

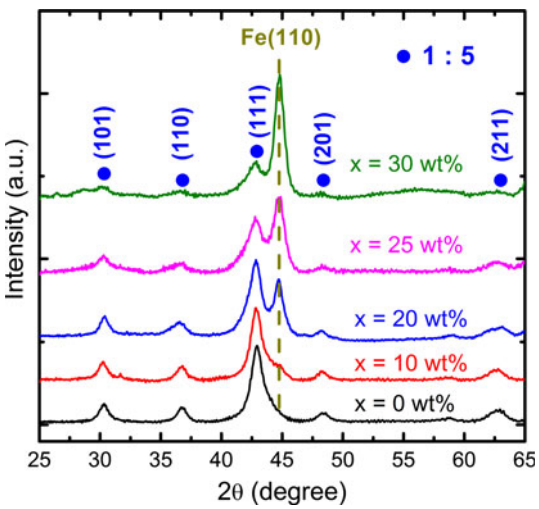

Fig. 7 XRD patterns of the samples with different Fe content

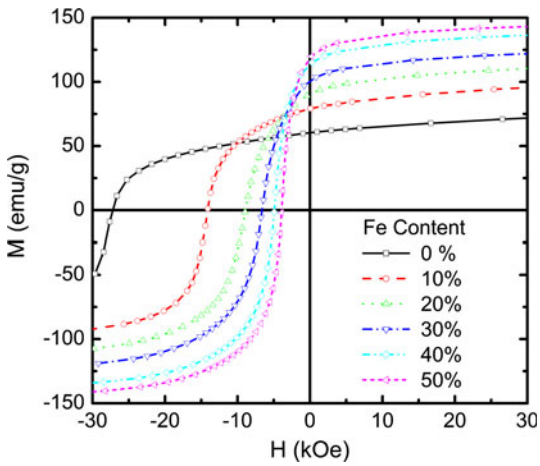

Fig. 8 Demagnetization curves of the SmCo/Fe nanocomposite with different Fe addition. Since the magnetization loops are symmetrical in shape, only the demagnetization halves are plotted

energy product of these materials degrades with even a small addition of the soft phase. We speculate that this degradation is caused by the complete solid-solution between Sm_2Co_{17} and Sm_2Fe_{17} phases. The pure Fe may have been completely consumed while Sm_2Fe_{17} will not provide either high magnetization or coercivity to the composites because of its very low Curie temperature and anisotropy.

Effect of compaction and interface conditions

The compaction process is another factor that plays an important role in defining magnetic performance of the nanocomposite magnet, since compacting time and temperature can both affect grain size and thus magnetic properties. Warm compaction of the nanocomposite magnets was performed at temperatures ranging from 20 to

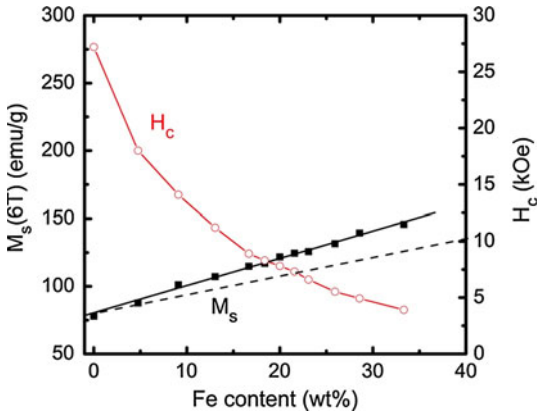

Fig. 9 Saturation magnetization and coercivity versus soft-phase content. The *dashed line* shows the magnetization according to Eq. 1 where no Co inter-diffusion is taken into consideration

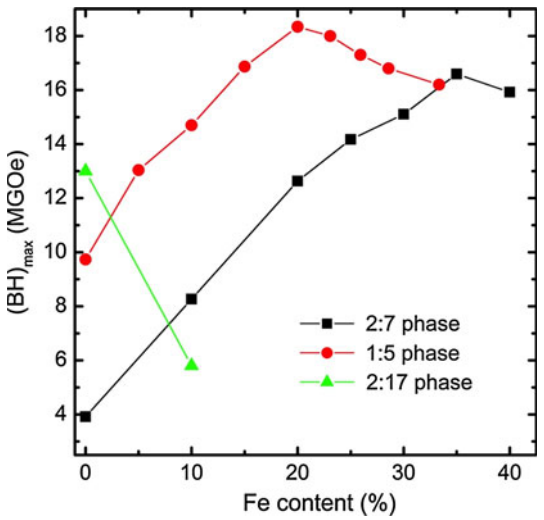

Fig. 10 Dependence of $(BH)_{max}$ on soft-phase content of the nanocomposite systems with different hard phases

700 °C, with the processing details described in our previous report [23]. Figure 12 shows the density and Vickers hardness dependence on the compaction temperature for the $SmCo_5$-based nanocomposite system. Both the density and hardness increase monotonically with increasing compaction temperature. When the compaction temperature is higher than 450–500 °C, the density and hardness change only slightly, which indicates that full densification of bulk magnets was achieved. However, the demagnetization curve shows a de-coupling behavior (signified as a kink) for compaction at temperatures above 600 °C (as given in Fig. 13) which is attributed to grain growth. Compaction at temperatures below 600 °C allows for a complete densification without excessive grain growth and therefore it produces nanostructured bulk materials with a controllable morphology. Figure 14 shows the dependence of the energy product on compaction temperature. The

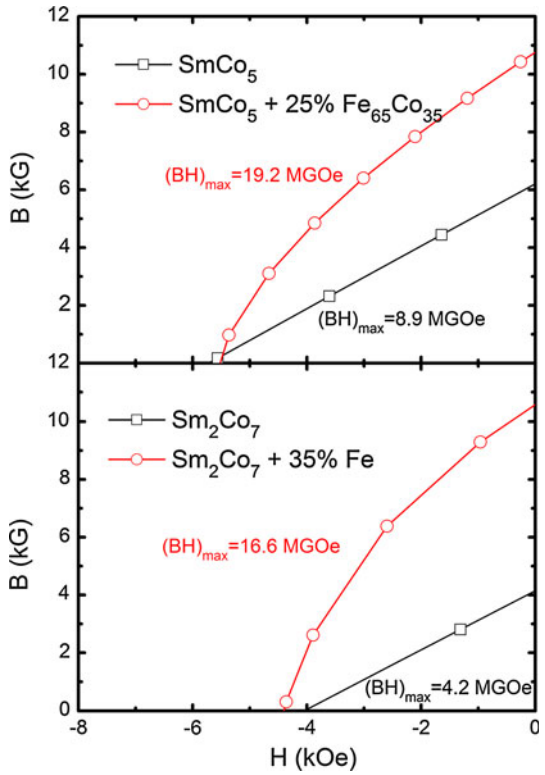

Fig. 11 The B–H curves of the $SmCo_5/Fe_{65}Co_{35}$ and Sm_2Co_7/Fe nanocomposite magnets with optimal energy products in comparison to their single-phase counterparts

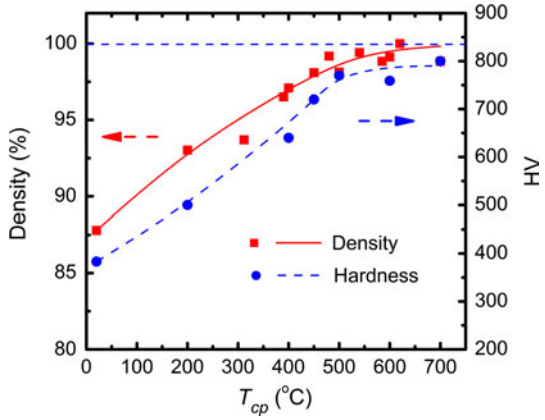

Fig. 12 Dependence of density and Vicker hardness of the $SmCo_5$/Fe bulk nanocomposite magnets on compaction temperature

highest energy product can be achieved at temperatures around 400 °C, obviously based on the limited grain size and the high density. For comparison, in Fig. 14 we also report the energy products of the single-phase $SmCo_5$ magnets produced under the same conditions. It can be seen that the energy product of the nanocomposite magnets is almost twice as high as that of the single-phase magnets.

Even when nanocomposites are compacted at a temperature at which grain growth is not observed, the

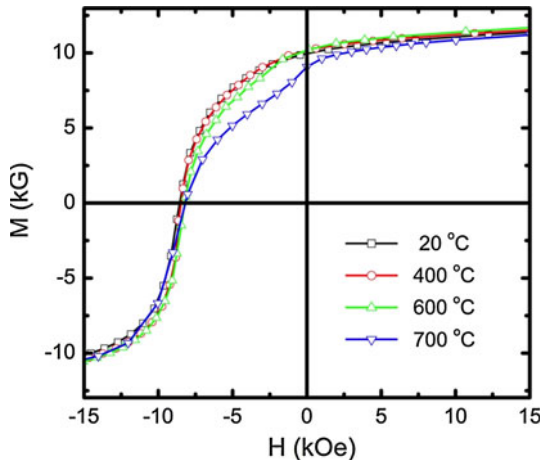

Fig. 13 Demagnetization curves of the bulk nanocomposite magnets prepared by compacting at different temperatures

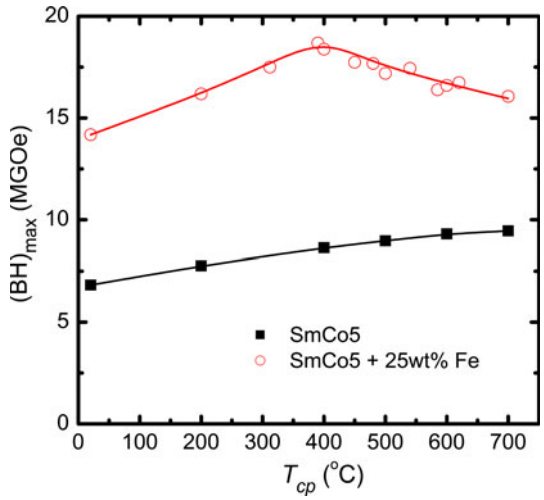

Fig. 14 Dependence of $(BH)_{max}$ of bulk single phase and nanocomposite magnets on compaction temperature

magnetic properties are still observed to depend on the pressure-holding times during the compaction. Figure 15 shows demagnetization curves of samples compressed at 500 °C for different pressure-holding times. A longer holding time increases the energy product by improving the coercivity and the squareness of the loops. The reason for this improvement can be attributed to the recent finding that inter-phase exchange coupling favors interdiffused interface (graded interface) [49, 50]. In other words, compositionally sharp interfaces should be avoided and a graded composition profile is desirable. We suspect that an extended pressure-holding at a modest temperature in our compaction processing facilitates the interdifussion of Co–Fe while avoiding a significant grain growth [25]. This interdiffusion is consistent with the wavelike composition profile of the soft phase in the bulk nanocomposite magnets observed using 3D atom probe and PEELS analyses, as

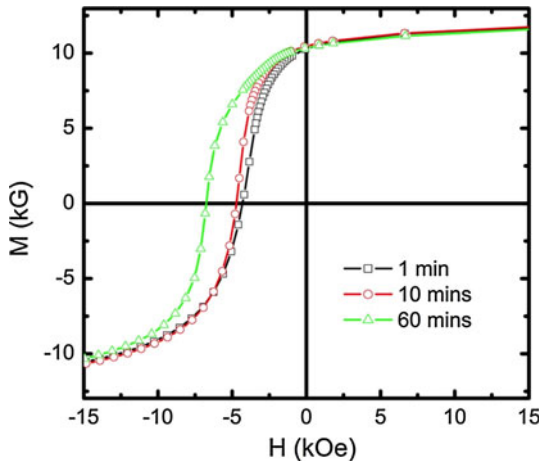

Fig. 15 Demagnetization curves of the bulk nanocomposite magnets prepared by holding the pressure for different time at 500 °C. Since the magnetization loops are symmetrical in shape, only the demagnetization halves are plotted

reported in Refs [24, 25]. Atom probe analysis also revealed that Fe-rich regions with dimensions smaller than 15 nm are distributed homogenously in the matrix of the hard phase.

Recognizing that Co diffusion into α-Fe resulted in a higher overall magnetization of the nanocomposites as compared to the case of the pure Fe soft phase, we adopted a second approach to compaction. Specifically, a pre-alloyed FeCo soft phase with a controlled composition (rather than pure Fe) was incorporated into the composite so that the final composition of the soft phase can reach $\sim Fe_{65}Co_{35}$, which has the highest magnetization among all the soft magnetic alloys. On the other hand, we found that adding Co into the soft phase can also reduce the Co loss from the hard phase. These new approaches allowed for further enhancements in the energy product. The $(BH)_{max}$ value for a $SmCo_5 + 25$ wt% $Fe_{65}Co_{35}$ nanocomposite is 19.2 MGOe, which represents a 115% enhancement as compared to the single-phase $SmCo_5$ magnet produced under the same conditions ($\sim$9 MGOe as shown in Fig. 11), and is also 7% higher than the nanocomposite with pure Fe addition (18.3 MGOe).

Conclusions

In conclusion, bulk SmCo/FeCo hard/soft nanocomposite magnets have been fabricated by means of intensive plastic deformation coupled with warm compaction. The mechanism of "self-nanoscaling", which is induced by plastic deformation, has been discovered in the magnetically and mechanically hard/soft composite systems. This mechanism can be used to produce nanocomposites with

the soft-phase inclusions that have a controllable size and are distributed homogenously. A giant energy product enhancement over the base single-phase materials (up to 300% for Sm_2Co_7 and up to 115% for $SmCo_5$) has been achieved in the isotropic nanocomposite systems. Up to 30% of α-Fe can be incorporated into the composites while keeping α-Fe particle size under 15 nm, which is below the critical length for effective inter-phase exchange coupling. By controlling the warm compaction process, it is possible to control interdiffusion between the phases. The refined hard–soft phase composite morphology is consistent with that predicted for ideal nanocomposite magnets: the soft phase is distributed homogenously in a hard-phase matrix in a wavelike composition profile.

Though challenges still remain in processing anisotropic bulk nanocomposite magnets with superior high energy products, our results have demonstrated the potential for producing high energy product bulk nanocomposite magnets in large scale that can be used at high temperatures. In addition, this type of Sm–Co–Fe based bulk permanent magnets will also lead to a significant reduction of cost due to the reduced Sm and Co contents in the materials as compared to traditional Sm–Co magnets. The processing technology used for preparing the materials can be applied to fabricate other bulk nanocomposite materials and can be readily scaled up for industrial productions.

Acknowledgements This work has been supported in part by the US Office of Naval Research/MURI project under Grant N00014-05-1-049, US DoD/DARPA/ARO under Grant W911NF-08-1-0249, and by the University of Texas-Arlington. Work at the Ames laboratory was supported in part by the US Department of Energy, Office of Basic Energy Science, under contract DE-AC02-07CH11358.

References

1. Buschow KHJ (1977) Rep Prog Phys 40:1179
2. Coehoorn R, Mooij DB, Waard C (1989) J Magn Magn Mat 80:101
3. Kneller EF, Hawig R (1991) IEEE Trans Magn 27:3588
4. Sellmyer DJ (2002) Nature 420:374
5. Skomski R, Coey JMD (1993) Phys Rev B 48:15812
6. Rong CB, Zhang HW, Chen RJ, He SL, Shen BG (2006) J Magn Magn Mater 302:126
7. Liu JP, Luo CP, Liu Y, Sellmyer DJ (1998) Appl Phys Lett 72:483
8. Liu W, Zhang ZD, Liu JP, Chen LJ, He LL, Liu Y, Sun XK, Sellmyer DJ (2002) Adv Mater 14:1832
9. Zhang J, Takahashi YK, Gopalan R, Hono K (2005) Appl Phys Lett 86:122509
10. Manaf A, Buckley RA, Davis HA (1993) J Magn Magn Mater 128:302
11. Withanawasam L, Hadjipanayis GC, Krause RF (1994) J Appl Phys 76:6646
12. Zhang XY, Guan Y, Yang L, Zhang JW (2001) Appl Phys Lett 79:2426
13. Ding J, McCormick PG, Street R (1993) J Magn Magn Mater 124:L1
14. Donnell O, Kuhrt C, Coey JMD (1994) J Appl Phys 76:7068
15. Zhang ZD, Liu W, Sun SK, Zhao X, Xiao Q, Sui Y, Zhao T (1998) J Magn Magn Mater 184:101
16. Zeng H, Li J, Liu JP, Wang ZL, Sun SH (2002) Nature 420:395
17. Nandwana V, Chaubey GS, Yano K, Rong CB, Liu JP (2009) J Appl Phys 105:014303
18. Rong CB, Nandwana V, Poudyal N, Li Y, Liu JP, Ding Y, Wang ZL (2007) J Phys D Appl Phys 40:712
19. Yue M, Zhang J, Tian M, Liu XB (2006) J Appl Phys 99:08B502
20. Mo W, Zhang L, Shan A, Cao L, Wu J, Komuro M (2007) Intermetallics 15:1483
21. Rong CB, Nandwana V, Poudyal N, Liu JP, Saito T, Wu Y, Kramer MJ (2007) J Appl Phys 101:09K515
22. Chen KH, Jin ZQ, Li J, Kennedy G, Zeng H, Cheng SF, Wang ZL, Thadhani NN, Liu JP (2004) J Appl Phys 96:1276
23. Rong CB, Nandwana V, Poudyal N, Liu JP, Kozlov ME, Baughman RH, Ding Y, Wang ZL (2007) J Appl Phys 101:023908
24. Rong CB, Zhang Y, Poudyal N, Xiong XY, Kramer MJ, Liu JP (2010) Appl Phys Lett 96:102513
25. Zhang Y, Kramer MJ, Rong CB, Liu JP (2010) Appl Phys Lett 97:032506
26. Chikazumi S (1997) Physics of ferromagnetism. Oxford University Press, Oxford, p 14
27. Hong MH, Hono K, Reynolds WT, Tarui T (1999) Metall Mater Trans A 30:717
28. Sevillano JG, García–Rosales C, Fuster JF (1999) Philos Trans R Soc Lond A 357:1603
29. Aernoudt E, Sevillano JG (1973) J Iron Steel Inst 211:718
30. Hellstern E, Schultz L (1986) Appl Phys Lett 49:1163
31. Shingu PH, Yasuna K, Ishihara KN, Otsuki A, Terauchi M (1997) Mater Sci Forum 235–238:35
32. Bordeaux F, Yavari AR (1989) J Appl Phys 67:2385
33. Atzmon M, Unruh KM, Johnson WL (1985) J Appl Phys 58:3865
34. Hebert RJ, Perepezko JH (2003) Scripta Mater 49:933
35. Chen IW, Winn EJ, Menon M (2001) Mater Sci Eng A 317:226
36. Vidal V, Thilly L, Lecouturier F, Renault PO (2006) Acta Mater 54:1063
37. Perepezko JH, Hebert RJ (2003) Z fur Metallkunde 94:1111
38. Semiatin SL, Piehler HR (1979) Metall Trans A 10:85
39. Hwang YM, Hsu HH, Lee HJ (1996) Int J Mach Tools Manufact 36:47
40. Junqua N, Grilhe J (1995) Philos Mag A 71:1125
41. Nowicke F, Zavaliangos A, Rogers HC (2006) Int J Mech Sci 48:868
42. Russell AM, Chumbley LS, Tian Y (2000) Adv Eng Mater 2:11
43. Yermakov AY, Yurchikov YY, Barinov VA (1981) Phys Met Metall 52:50
44. Williamson K, Hall WH (1953) Acta Metall 1:22
45. Krommuler H, Fisher R, Bachmann M, Leinewber T (1999) J Magn Magn Mater 203:12
46. Shan ZS, Liu JP, Chkka VM, Zeng H, Jiang JS (2002) IEEE Trans Magn 38:2907
47. Guo ZJ, Jiang JS, Pearson JE, Bader SD, Liu JP (2002) Appl Phys Lett 81:2029
48. Liu JP (2009) In: Liu JP, Fullerton E, Gutfleisch O, Sellmyer DJ (eds) Nanoscale magnetic materials and applications. Springer, New York, p 316
49. Jiang JS, Pearson JE, Liu ZY, Kabius B, Trasobares S, Miller DJ, Bader SD, Lee DR, Haskel D, Srajer G, Liu JP (2004) Appl Phys Lett 85:5293
50. Choi Y, Jiang JS, Ding Y, Rosenberg RA, Pearson JE, Bader SD, Zambano A, Murakami M, Takeuchi I, Wang ZL, Liu JP (2007) Phys Rev B 75:104432